Original Research

Effective Photogeneration of Singlet Oxygen and High Photocatalytic and Antibacterial Activities of Porous Mn-Doped ZnO-ZrO₂ Nanocomposites

Sergey Evstropiev [1, 2, †, *], Andrey Shelemanov [1, †], Igor Bagrov [1, †], Anna Karavaeva [2, †], Ksenya Portnova [1, †], Nikolay Nikonorov [1, 2, †]

1. ITMO University, Kronverskiy pr., 49, St. Petersburg, Russia; E-Mails: evstropiev@bk.ru; shelemanov@mail.ru; i.bagrov2@gmail.com; Ksiu.san@gmail.com; nikonorov@oi.ifmo.ru
2. St.Petersburg State Technological Institute (Technical University), Moskovskii pr., 26, St. Petersburg, Russia; E-Mail: ann-karavaeva@yandex.ru

† These authors contributed equally to this work.

* **Correspondence:** Sergey Evstropiev; E-Mail: evstropiev@bk.ru

Abstract

Disperse porous Mn-doped ZnO-ZrO₂ nanocomposites were prepared using the facile polymer-salt method. The effect of Mn content on the crystal structure, composite morphologies, their ability to photogenate the singlet oxygen, luminescence properties, and bactericidal activities were studied. The crystal structure and morphology of these materials were investigated using XRD and SEM analysis. It was found that obtained nanocomposites consist of small (~9 nm) hexagonal ZnO and fine ZrO₂ crystals and the embedding of Mn ions expands the crystal cells of ZnO crystals. Photoluminescence spectra indicate the presence of different structural defects (interstitial Zn ions and oxygen vacancies in ZnO and oxygen vacancies in ZrO₂ crystals). Mn-doped ZnO-ZrO₂ nanocomposites can photogenerate singlet oxygen under visible (λ = 405 nm) irradiation. The increased power density of the exciting blue (λ = 405 nm) light significantly enhances the singlet oxygen photogeneration by prepared

composites. The dependence of the intensity of singlet oxygen photogeneration by composites on the power density of exciting radiation (at its variation in the range $0.8 \div 1.6$ W/cm^2) is close to linear. Mn-doped ZnO-ZrO$_2$ composites demonstrate superior antibacterial activity against the gram-positive bacteria *Staphylococcus aureus ATCC 209P*. It was found that highly dispersed porous Mn-doped ZnO-ZrO$_2$ nanocomposites are promising for practical environmental and medical applications.

Keywords
Ceramics; nanocomposites; crystal; bacteria; ZnO

1. Introduction

Photocatalytic and bactericidal metal oxide materials are the object of intensive investigations. Numerous oxide semiconductor materials are effective photocatalysts, demonstrate antibacterial activity and have excellent thermal stability and chemical durability.

Reactive oxygen species (ROS) are a set of unstable molecules, including hydrogen peroxide (H_2O_2), hydroxyl radical (OH^-), singlet oxygen ($^1O_2$) and superoxide (O_2^-) that are produced by all kinds of cells in living organisms [1-6]. According to [2, 3], four major ROS are recognized, comprising superoxide ($\cdot O_2^-$), hydrogen peroxide (H_2O_2), hydroxyl radical ($\cdot OH$), and singlet oxygen ($^1O_2$), but they display very different kinetics and levels of activity [3]. The effects of O_2^- and H_2O_2 are less acute than those of OH and $^1O_2$ because the formers are much less reactive. The hydroxyl radical demonstrates the highest antibacterial activity, and it is a highly aggressive oxidant. as such, it can attack various biological molecules and impair their proper functioning [3]. The energy consumed for ROS generation also depends on their types. According to [1], the ability to generate different ROS types by metal oxides is related to their band gap values and the redox potentials of the various ROS formations.

The interaction between ROS and bacteria is critical in the antibacterial action of oxide materials [3, 4, 7]. Therefore, generating chemically active oxygen species is especially important for bactericidal oxide materials. The effectiveness of ROS generation depends on the chemical composition of semiconductor materials, their structure and morphology and can be significantly enhanced by light irradiation [7, 8]. The mechanisms of ROS antibacterial action were described in detail in [1, 2, 7, 9].

The biochemical processes that determine the antibacterial effect of oxide materials occur both under external light irradiation and in the dark [8]. The authors [8] showed that the antibacterial activity of ZnO-based nanoparticles is significantly higher in natural lighting than in darkness. The antibacterial activity of ZnO nanoparticles might involve both the production of reactive oxygen species and the accumulation of nanoparticles in the cytoplasm or on the outer membranes [9].

ROS are produced in energy-demanding conditions [10], and photogeneration plays a vital role in the antibacterial activity of semiconductor materials [1, 11]. The effectiveness of this process depends on the parameters of excited radiation (intensity, wavelength, etc.) [4, 12].

Oxide composites of two or more various closely packed semiconductor particles demonstrate higher bactericidal properties than pure oxides [3, 4]. Using these heterostructures decreases the

possibility of the recombination of photogenerated electron-hole pairs by the charge's spatial separation [13, 14]. Also, the interaction between different oxide particles stimulates the formation of structural defects in their structures. These defects play the important role in photocatalytic and bactericidal properties of oxide materials [14-16]. The defect centers in the structure of semiconductor oxide, forming the electronic levels inside its band gap, modifying the electronic structure, and playing an important role in the material's antibacterial properties [14, 16]. The study of luminescence spectra allows for the identification of these defects and specifies the electronic structure of semiconductor materials.

Different materials (powders, coatings, composites) based on ZnO demonstrate high photocatalytic properties and antibacterial activity [5, 8, 9, 12, 13, 17, 18]. Modification of ZnO-based materials by other oxides significantly enhances their bactericidal characteristics. These additions decrease the size of ZnO crystals, increase their specific surface areas and modify the crystal and electronic structures and morphology of ZnO materials.

ZrO_2 as a broad bandgap (~5.10 eV) semiconductor has been widely explored due to the presence of many oxygen vacancies on the surface, significant ion exchangeability and physiochemical stability [14, 19].

It is known [20-22] that different, closely disposed of crystals (such as ZnO and ZrO_2) prohibit the growth of each to other during their simultaneous crystallization. This phenomenon leads to nanocomposites with high specific surface areas and improved photocatalytic and bactericidal properties [22]. $ZnO-ZrO_2$ materials demonstrate photocatalytic [23-26] and bactericidal [27] properties.

In [28, 29] Mn additions are used to modify ZnO and ZrO_2. The application of Mn doping can enhance the photocatalytic activity of $ZnO-ZrO_2$ composites due to the reduction of their band gap values [30]. Also, embedding Mn ions into oxide crystals is often accompanied by the deformation of their lattices [28, 31]. This process leads to different structural defects that affect the photocatalytic and antibacterial activities of materials [14, 16]. Thus, Mn-doped nanocomposites $ZnO-ZrO_2$ could be promising for photocatalytic and bactericidal applications. Therefore, these materials were the object of this study.

Many methods have been developed for the preparation of nanocrystalline ceramic $ZnO-SnO_2$ photocatalysts: co-precipitation [14, 32], polymer-salt technique [8, 12], electrospinning method [19], etc. [18]. Polymer-salt synthesis is a facile and effective method used to prepare different ZnO-based nanomaterials [8, 12]. In this method, aqueous solutions of thermally decomposable metal salts and soluble polymer were used as oxide nanoparticle precursors.

Polycrystalline materials obtained by polymer-salt synthesis have porous structures providing effective contact with the surrounding media and high adsorptive, photocatalytic and bactericidal properties [33-35]. Porous oxide materials have high values of specific surface areas, and many of them demonstrate superior antibacterial properties and photocatalytic activity [35]. Porous Mn-doped $ZnO-ZrO_2$ composites could be especially promising for photocatalytic and medical applications. Therefore, using facile polymer-salt synthesis for their preparation could be promising. To our knowledge, this method hasn't been used to synthesize photocatalytic Mn-doped $ZnO-ZrO_2$ nanocomposites.

This work aims to design the chemical synthesis of effective bactericidal Mn-containing $ZnO-ZrO_2$ nanocomposites and their characterization. The used approach of nanocomposite development included the study and design of their morphology and crystal structure for the enhancement of

luminescent properties, the ability to ROS photogeneration, and the improvement of bactericidal properties.

2. Materials and Methods

2.1 Synthesis

Polymer-salt technique was used for the preparation of powder samples. Aqueous solutions of $Zn(NO_3)_2$, $Zr(NO_3)_4$ and $MnSO_4$ in pre-determined volumes were mixed at room temperature with the solution of polyvinylpyrrolidone ((PVP), M_w = 25000 ÷ 35000). The mixed solution was dried at 70°C for 24 hours to prepare the polymer-salt composite. Then, the polymer-salt composites that were obtained were subjected to thermal treatment at 600°C for 2 hours in an air atmosphere. Nominal chemical compositions of powder samples are given in Table 1.

Table 1 Chemical composition of Mn-doped ZnO-ZrO_2 composites.

Sample	Nominal chemical composition, mol/%		
	ZnO	ZrO$_2$	MnO (above 100%)
ZnZr	90	10	-
ZnZrMn0.5	90	10	0.5
ZnZrMn1	90	10	1.0
ZnZrMn2	90	10	2.0

2.2 Characterization

The crystal structure of prepared powders was investigated by the XRD method using the device Rigaku Ultima IV. The diffraction patterns were scanned from 20° to 100° (2θ). Based on the obtained XRD data, we estimated the crystal sizes using the Scherrer formula:

$$d = \frac{K \times \lambda}{\beta \times cos\theta},$$

(1)

where d is the average crystal size; K is the dimensionless particle shape factor (for spherical particles K = 0.9); λ is the X-ray wavelength (λ (CuKα = 1.5418 Å); β - is the width of the reflection at half height (in radians, and in units of 2θ); θ is the diffraction angle.

The morphology and chemical composition of prepared samples were studied by SEM and energy-dispersive analysis using the electronic microscope TESCAN VEGA3 equipped with the setup for energy-dispersive analysis Advanced Aztec Energy (Oxford Instruments).

Photoluminescence spectra in near IR spectral region were measured upon excitation by the radiation of LEDs (HPR40E set) with emission bands maximums at 370 nm and 405 nm using a spectrometer SDH-IV (SOLAR Laser Systems). The luminescence spectra in UV and visible spectral ranges were measured using the spectrofluorometer Perkin Elmer LS50B.

2.3 Antibacterial Activity

The method described in [5, 8] was used to estimate the bactericidal properties of prepared coatings. The Gram-positive bacteria *Staphylococcus aureus ATCC 209P* was applied as a test

bacteria. Bactericidal activity was assessed by measuring the size of an inhibited area formed on surface containing bacteria.

2.4 Dye Adsorption and Photocatalytic Decomposition

Diazo dye Chicago Sky Blue (CSB) (Sigma Aldrich) was used as a model organic contaminant for the estimation of adsorption and photocatalytic properties of obtained composites. This dye is applied widely in the textile industry [36] and was used previously to study different materials' photocatalytic and adsorption properties [30, 34, 35]. The adsorption and photocatalytic properties of powders were studied in their suspensions, which were prepared by adding 0.01 g of the powder to 3 ml of the aqueous solution of CSB dye (0.042 g/l). The quartz cuvettes were filled with these suspensions and were kept in the darkness during dye adsorption experiments. The amount of adsorbed or photocatalytic decomposed dye was determined by a spectrophotometric method based on the changes in the light absorption of the solution at a wavelength corresponding to the maximum of the absorption band of the dye.

Mercury lamp (λ_{max} = 254 nm) (DR-240, Russia) was used for UV irradiation of the cuvette with dye solution. Blue LED (λ = 405 nm) was used for photocatalytic experiments under visible irradiation. The cuvette was disposed of at a distance of 7 cm from the LED. The power density of exciting visible light during these experiments was 50 mW/cm^2.

3. Results

3.1 XRD Analysis

Figure 1 demonstrates XRD patterns of composites ZnZr (a) and ZnZrMn2 (b). The comparison of these patterns indicates that small Mn additions do not remarkably affect the crystal structure of the ZnO-ZrO$_2$ composite. Intensive peaks of hexagonal ZnO crystals and small peaks of ZrO$_2$ crystals are observed in both XRD patterns. The small content of ZrO$_2$ in composites, low intensities of its peaks, and their overlapping with peaks of ZnO crystals prohibits the identification of ZrO2 crystal structures. It is worth noticing the absence of any peaks of Mn compounds in the diffractogram of the ZnZrMn2 composite (Figure 1b).
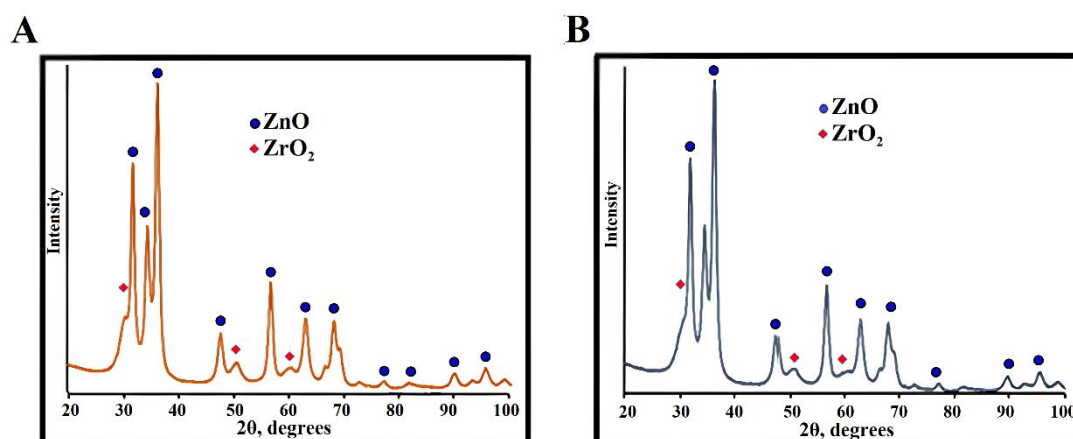

Figure 1 Diffraction patterns of composites ZnZr(a) and ZnZrMn2 (b).

Figure 2 shows the distribution of ZnO crystals in prepared materials based on their size. It can be seen that all materials are characterized a narrow crystals size distribution and average crystallite size in all powders is about 9 nm. Obtained data show that Mn addition doesn't change the size of ZnO crystals.
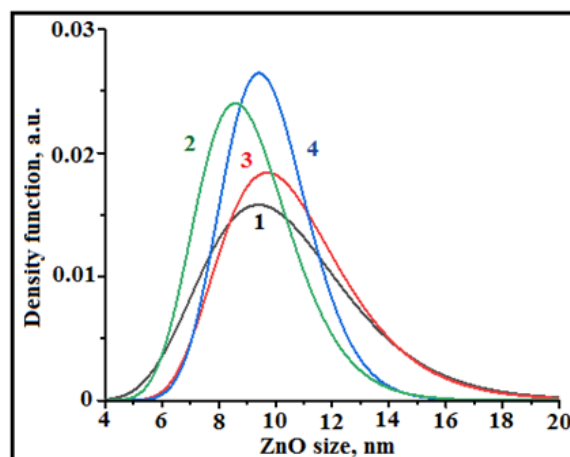

Figure 2 Distribution of ZnO crystals on their size in composites: ZnZr (curve 1); ZnZrMn0.5 (curve 2); ZnZrMn1 (curve 3); ZnZrMn2 (curve 4).

The ionic radius of Mn^{2+} is slightly bigger than the ionic radius of Zn^{2+} (0.80 and 0.74 Å, correspondingly), but the difference is slight and Mn^{2+} ions can replace Zn^{2+} in ZnO crystal lattice [31]. Crystal cell parameters of ZnO crystals in prepared composites and in different materials previously described in the literature are given in Table 2. These data show that Mn addition leads to the remarkable deformation of ZnO crystal cells. The crystal cell parameter *a* remains its value, but the parameter *c* significantly increases. A similar phenomenon was observed previously in [28, 31]. Such behavior of the crystal cell deformation can be explained by the lower density of chemical bonds along the *c* axe direction in the ZnO crystal cell (Scheme 1), which determines its flexibility in this direction.

Table 2 Parameters of ZnO crystal cell in varied materials.

Sample	a, Å	c, Å	V, Å³	c/a	Reference
ZnZr	3.2518	5.2196	47.7972	1.6051	Present study
ZnZrMn0.5	3.2498	5.2278	47.8135	1.6087	Present study
ZnZrMn1	3.2501	5.2266	47.8113	1.6081	Present study
ZnZrMn2	3.2488	5.2321	47.8233	1.6105	Present study
ZnO	3.2496	5.2042	-	1.6018	[37]
ZnO	3.2501	5.2071	47.63	1.6021	[38]
ZnO	3.2487	5.1989	47.52	1.6003	[28]
ZnO (Mn1)	3.2500	5.2030	47.59	1.6009	[28]
ZnO (Mn5)	3.2493	5.2023	47.57	1.6010	[28]
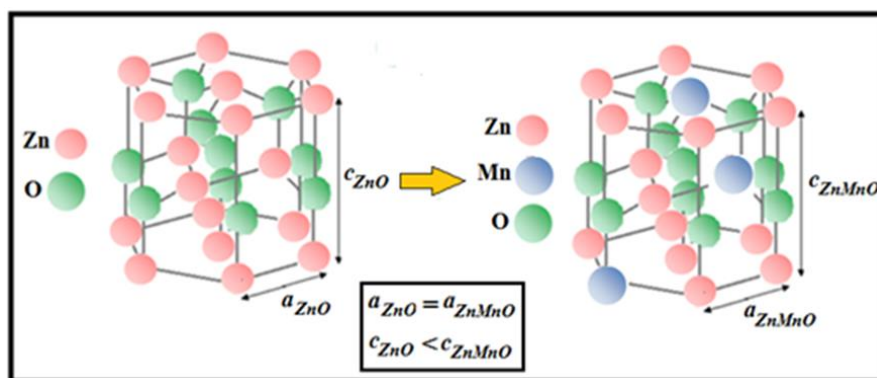
Scheme 1 The scheme illustrating the change of the ZnO crystal cell at the embedding of Mn ions. Thus, XRD data indicate the formation of hexagonal ZnO crystals as the main crystal phase in the obtained powders. The embedding of Mn ions deforms the crystal cells of ZnO crystals, which can promote their structural defect formation.

3.2 SEM Analysis

Figure 3 demonstrates SEM images of composite ZnZrMn1 at different magnification values. The photo shows that the composite contains a big porous aggregate that is tens of microns in size (Figure 3a). These aggregates consist of small nanoparticles (Figure 3b).
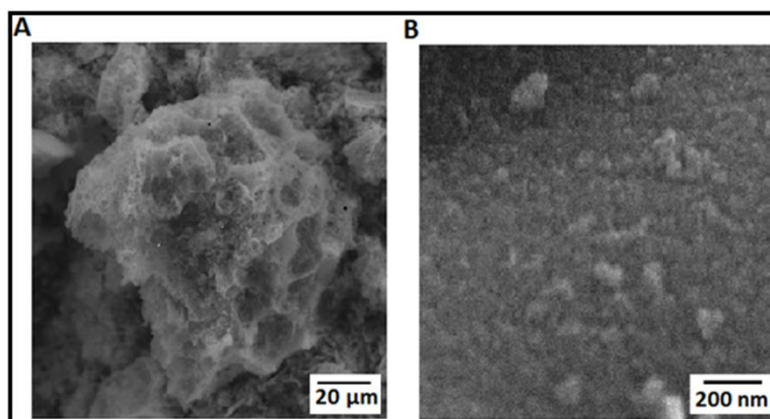

Figure 3 SEM images of composite ZnZrMn1 at different magnification values.

3.3 Luminescence

3.3.1 Luminescence in NIR Spectral Range

The photoluminescence spectrum of the ZnZrMn1 composite in the NIR range is shown in Figure 4. The luminescence band characteristic for the singlet oxygen ($^1\Delta_g$-$^3\Sigma_g$ electronic transition [39]) is observed in the spectrum. It is worth noticing that the singlet oxygen generation proceeds under blue light (λ_{ex} = 405 nm) excitation.
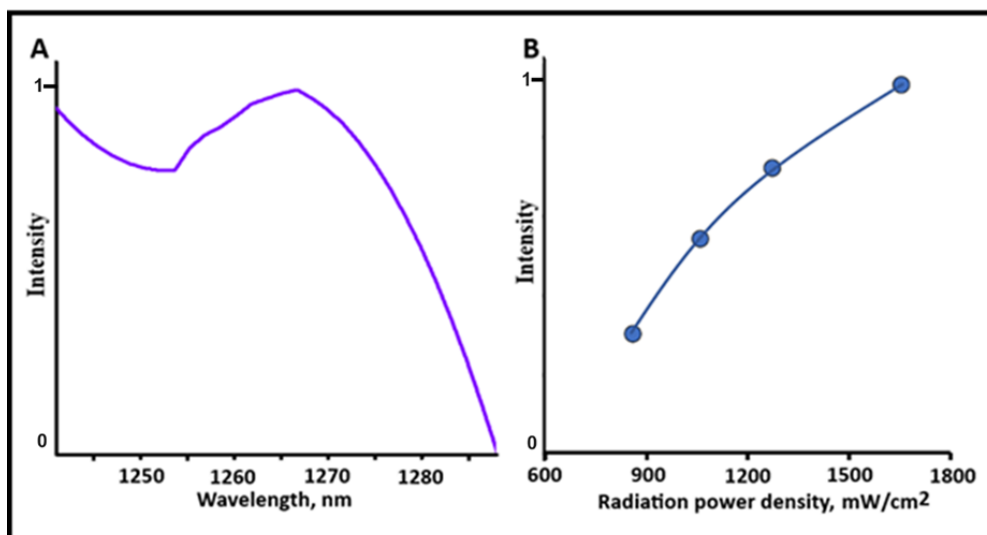
Figure 4 Photoluminescence spectrum of composite ZnZrMn1 (a). Dependence of the luminescence intensity from the excited radiation density (b).

The increase in visible light intensity enhances singlet oxygen generation (Figure 4b). The observed dependence of the luminescence band (λ = 1270 nm) intensity I_{SO} from the intensity of excited visible irradiation (λ_{ex} = 405 nm) I_{ex} is not linear. The similar dependence was observed earlier for the ceramic ZnO-SnO_2-Fe_2O_3 coating [12]. The non-linear behavior of the dependence is determined by the significant increase in the recombination of photogenerated electron-hole pairs at the growth of the excited radiation intensity [40].

3.3.2 Luminescence in Near UV and Visible Spectral Range

The main components of prepared composites can demonstrate photoluminescence (PL) related to different structural defects in near UV and visible spectral ranges. The luminescence ZrO_2 observable at room temperature is from defect states. The number of luminescence bands peaking within the spectral region from about 350 nm to 620 nm varies from one to eight [41, 42].

In PL spectra of ZnO-based materials are often observed the excitonic emission band located at $365 \div 370$ nm and luminescence peaks in visible range attributed to different structural defects of ZnO crystals [43].

Figure 5 demonstrates PL spectra of composites ZnZr (a) and ZnZrMn1 (b) at the excitation by UV-C (λ_{ex} = 256 nm) (Figure 5a) and UV-A (λ_{ex} = 356 nm) (Figure 5b) and blue (λ_{ex} = 407 nm) light (Figure 5c). The small peak at 343 nm attributed to the structural defects in ZrO_2 nanoparticles, was observed earlier [44].
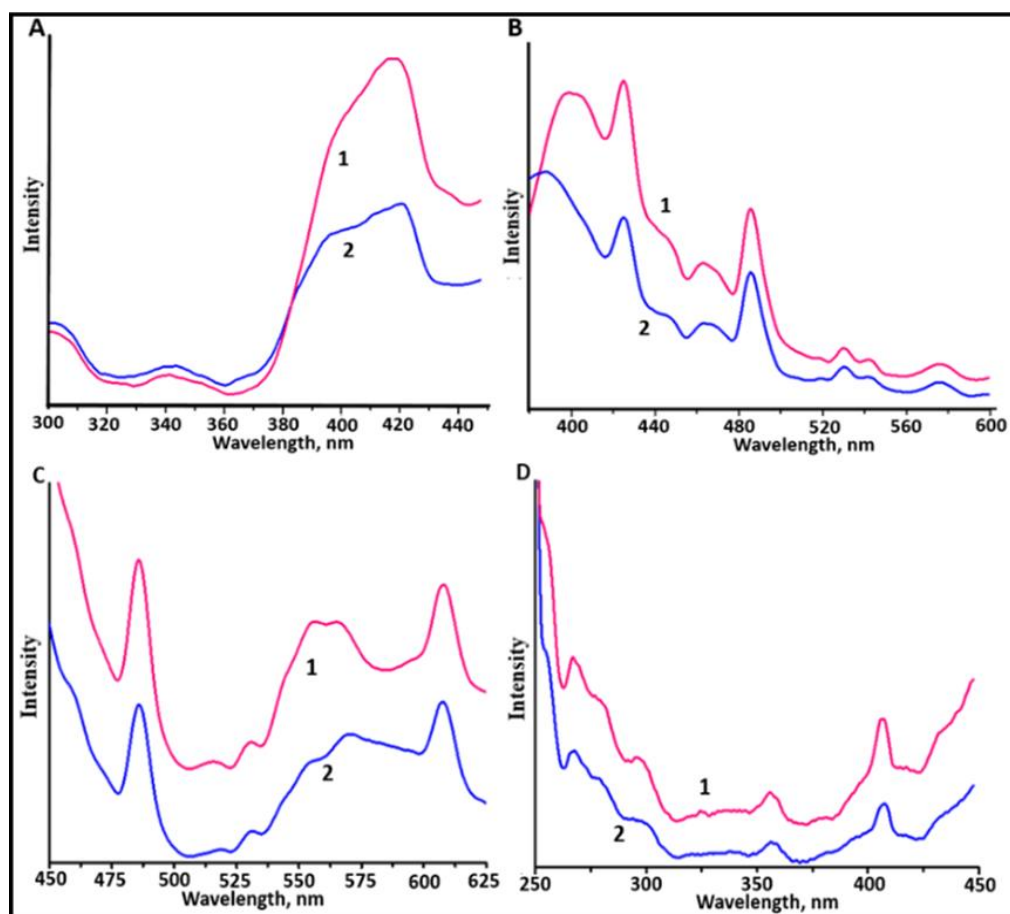
Figure 5 Photoluminescence spectra of composites ZnZr (curve 1) and ZnZrMn1 (curve 2). Excitation wavelength 256 nm (a); 357 nm (b); 407 nm (c). Luminescent excitation spectrum of composites ZnZr (curve 1) and ZnZrMn1 (d) (curve 2). Emission wavelength 487 nm.

The complicated shape of the luminescent band with λ_{max} ~415 nm suggests that it is a result of overlapping a few different luminescent peaks. The intensive luminescence band with λ_{max} ~415-420 nm was observed in the spectra of ZrO_2 nanoparticles at UV-C light excitation [32, 42, 44]. Also, Zn interstitials - structural defects in ZnO crystals have emission bands with λ_{max} = 415, 440, and 455 nm [43, 45].

In [46] the peaks with λ_{max} = 385 and 442 nm tentatively ascribed to singly ionized oxygen-vacancy defects and singly ionized associated oxygen vacancy defects attributed to ionized oxygen-vacancy defects were observed in ZrO_2 nanopowders.

Emission peaks with λ_{max} = 460 and 485 nm attributed to ZrO_2 structural defects were observed previously in [32, 44, 47] and were attributed to oxygen vacancies in ZrO_2 crystals [47]. PL peaks at ~530 nm and 608 nm were observed earlier in PL spectra at the excitation of tetragonal ZrO_2 nanocrystals by blue light (λ_{ex} = 412 nm) [42].

The luminescence observed in the spectral range 525 ÷ 575 nm corresponds to oxygen vacancies in the structure of ZnO crystals [48]. The absorption bands of structural defects in ZrO_2 crystals are observed in UV diapason in the luminescence excitation spectrum of composites (Figure 5d).

According to these experimental results on the luminescence spectra, different defects are present in the nanocomposites that were obtained. According to the experimental results reported

previously by GuO L. et al. [49], significant part of structural defects in ZnO nanocrystals are disposed on the surface. Photocatalytic effect occurs on the surfaces of materials. Therefore, the input of the surface structural defects in the excitation of formed nanocrystals by visible irradiation can be remarkable.

Thus, the measurements of photoluminescence spectra showed the presence of numerous different intrinsic defects (oxygen vacancies, interstitials Zn ions, etc.) in the structures of ZnO and ZrO_2 crystals.

3.4 Changes in Spectral Properties of Dye Solutions during the Adsorption and Photocatalysis

Figure 6 illustrates changes in absorption spectra of dye solutions during the adsorption process (a) and photocatalysis (b) in the presence of nanocomposite ZnZrMn0.5. The views of spectral changes of dye solutions are similar, and the shapes of the spectra remain the same during both processes.
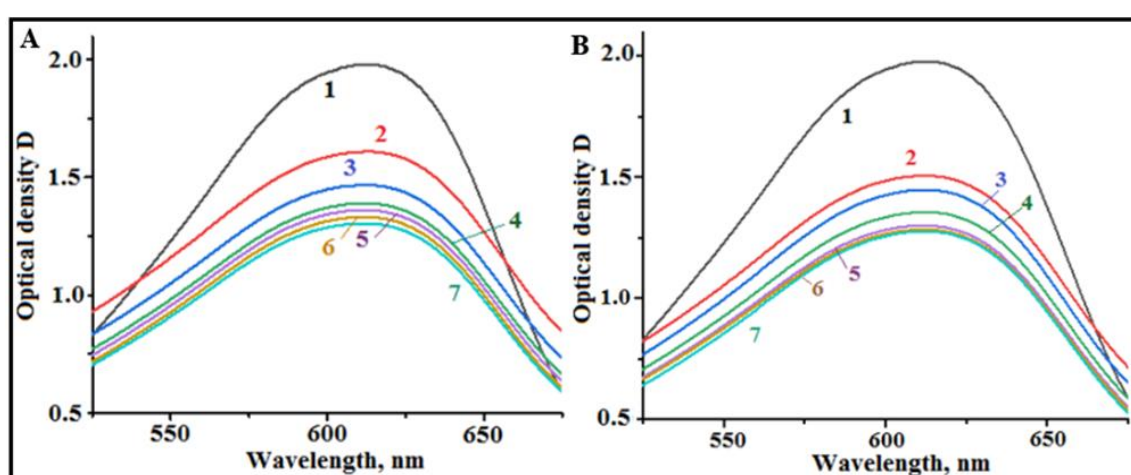

Figure 6 Changes of absorption spectra of dye solutions during adsorption process (a) and photocatalysis (b) in the presence of nanocomposite ZnZrMn0.5. Durations of these processes, min.: 0 (curves 1); 5 (curves 2); 10 (curves 3); 15 (curves 4); 20 (curves 5); 25 (curves 6); 30 (curves 7).

The CSB dye oxidative decomposition mechanism in aqueous solutions includes forming intermediate products. In [36] it was suggested that diazene derivatives and quinone are the intermediate products at the CSB dye oxidative decomposition in aqueous solutions in the presence of a purified laccase. The structure of diazine derivatives was represented in [50] by the general formula shown in Figure 7. In this formula, **n** represents an integer, at least 1 and not more than 3, **Y** represents oxygen or sulfur, and **R** - hydrogen, monovalent hydrocarbon or halo-hydrocarbon radicals.
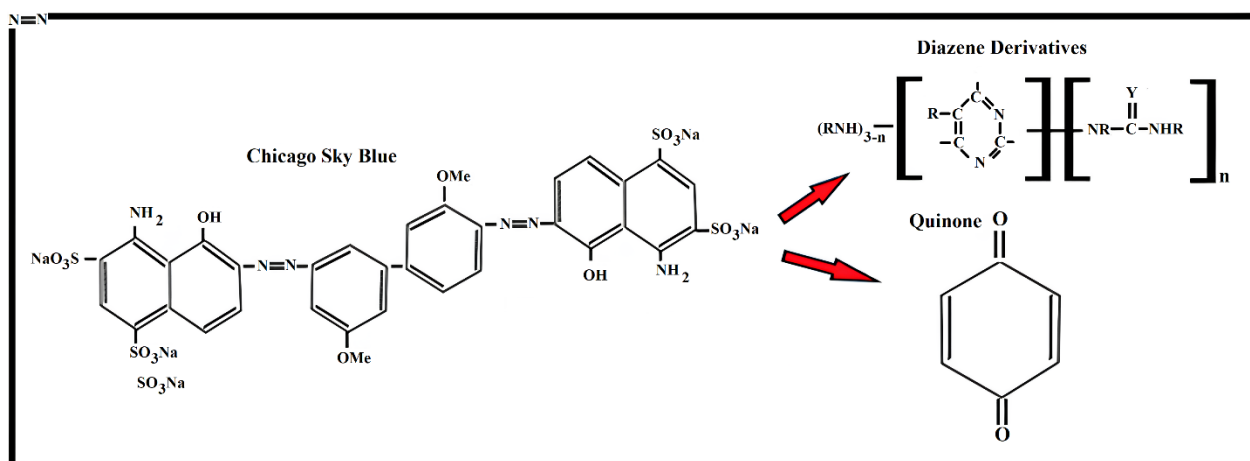
Figure 7 Illustrates the formation of some intermediate products during the oxidative decomposition of CSB dye in an aqueous solution. The scheme is based on the data reported in [36].

Based on the data reported in [33], the scheme of oxidative decomposition of CSB molecules in an aqueous solution can be presented as:

According to the results described in [36], the light absorption by formed intermediate compounds is one order lower compared with parent CSB molecules. It determines the weak changes in the shape of absorption spectra during the photocatalytic decomposition of CSB dye (Figure 6b).

Figure 8a demonstrates the comparison of kinetic dependencies of discoloration of dye solution during the adsorption process on the surface of nanocomposite ZnZrMn0.5 (curve 1) and photocatalysis under visible irradiation (curve 2) in the presence of this nanocomposite. The rate of the photocatalytic process is somewhat higher than the adsorption rate at the initial stage of these processes (during about the first 5 min.). Later, the rates of these processes are approximately equal to each other.
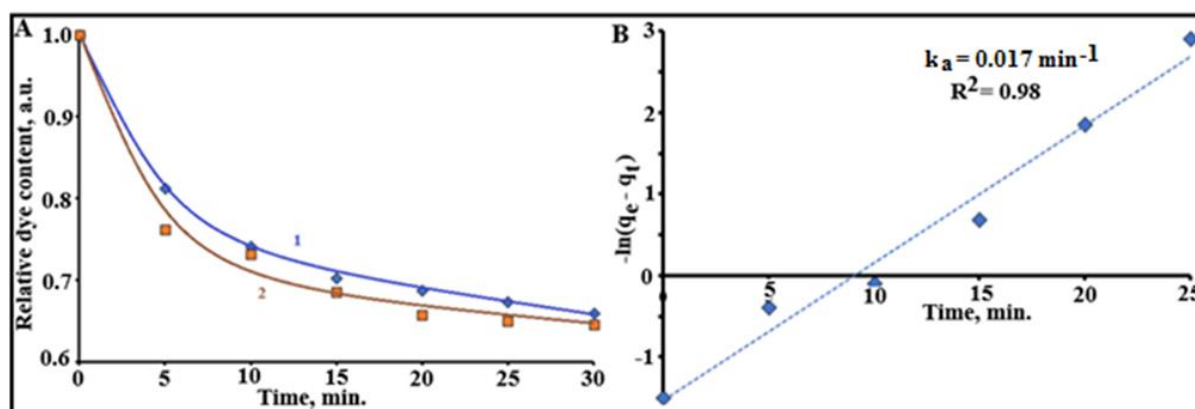

Figure 8 a) The comparison of kinetic dependencies of discoloration of dye solution during adsorption process on the surface of nanocomposite ZnZrMn1 (curve 1) and photocatalysis under visible irradiation (curve 2) at the presence of this nanocomposites; b) Dependence $-\ln(q_e-q_t) = f(t)$ for the CSB adsorption on the surface of ZnZrMn1 powder.

The kinetics of the dye adsorption on the surface of photocatalysts is often described using the kinetic model of pseudo-first order [30, 35, 51]:

$$\frac{dq_t}{dt} = k_a(q_e - q_t), \tag{2}$$

where q_t (mg/g) - the amount of the dye, adsorbed by 1 g sorbent during t min; q_e - equilibrium adsorption capacity of the sorbent (mg/g); k_a (min^{-1}) - the rate constant of the adsorption; t - adsorption duration (min). According to equation (1), the adsorption rate decreasess as the sorbent surface is filled with dye molecules, and the q_e value corresponds to the sorbent's equilibrium adsorption capacity. It is worth noticing that the dye adsorption proceeds fast ($k_a = 0.017$ min^{-1}). The values of CSB adsorption rate constants reported in [52-54] for other ZnO-based composites are significantly less.

3.5 Photocatalytic Activity

Experiments showed that both prepared nanocomposites demonstrate high photocatalytic activity under UV irradiation. The rate of photocatalytic dye decomposition depends on the radiation intensity. Figure 9a illustrates the effect of the intensity of UV light on the kinetic dependencies of CSB decomposition in the presence of composite ZnZrMn0.5. Similar results were obtained for all prepared Mn-doped ZnO-ZrO$_2$ composites. The increase of Mn concentration in the composites leads to some enhancement of their photocatalytic activity.
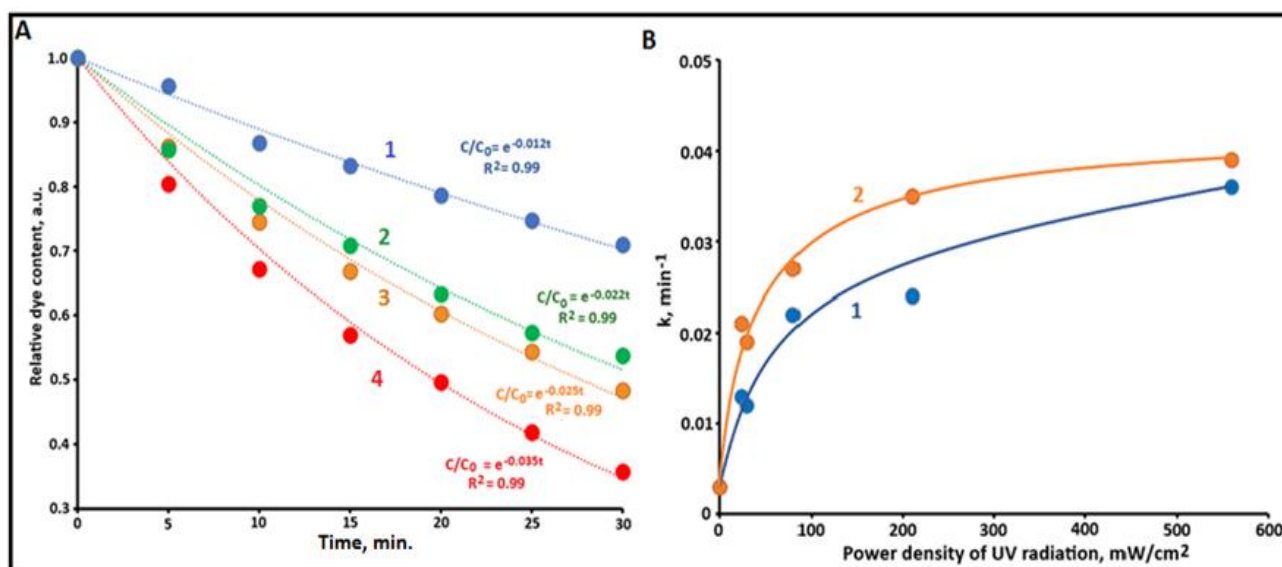

Figure 9 a) Kinetic dependencies of dye photocatalytic decomposition by the composite ZnZrMn0.5 under UV irradiation with different UV light intensities; b) Dependences of the rate constant of photocatalytic degradation of an organic dye by ZnZrMn0.5 (curve 1) and ZnZrMn1 (curve 2) composites on the power density of UV radiation.

Figure 9b shows the dependences of rate constant k of photocatalytic degradation of organic dye by the composites ZnZrMn0.5 and ZnZrMn1 on UV radiation's power density (I_{ex}). The decomposition rates grow with the increase of the radiation intensity, but observed dependencies k = f(I_{ex}) are not linear.

Figure 10a presents the kinetic dependencies of photocatalytic dye decomposition in the presence of prepared composites under visible (λ_{ex} = 405 nm) irradiation. The photocatalytic treatment for 30 min decreases the dye content in the solution by up to 50%. Experimental results show that the general tendency is that the increase of Mn content in composites enhances their photocatalytic activities.
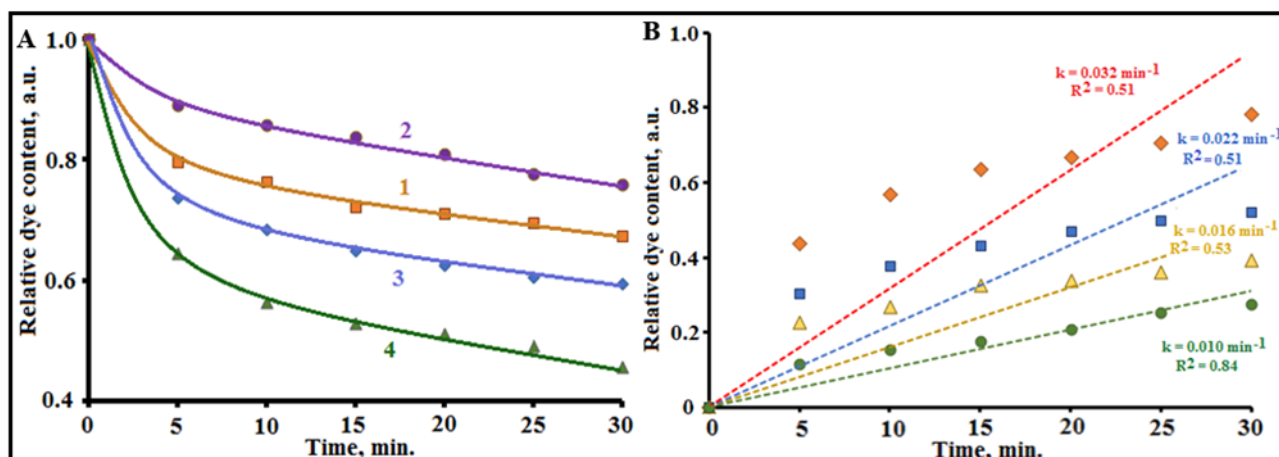

Figure 10 a) Kinetic dependencies of dye photocatalytic decomposition by composite ZnZr (curve 1); ZnZrMn0.5 (curve 2); ZnZrMn1 (curve 3); ZnZrMn2 (curve 4) under visible irradiation; b) Dependences - ln(C/C$_0$) = f(t) for the dye photocatalytic decomposition by composite ZnZr (curve 1); ZnZrMn0.5 (curve 2); ZnZrMn1 (curve 3); ZnZrMn2 (curve 4) under visible irradiation.

The remarkable feature of kinetic dependencies shown in Figure 10a is the sharp decrease of dye contents in solutions during the photocatalytic process's initial stage (during the first 5 min). After 10-15 min, the rate of dye decomposition decreases remarkably. A similar phenomenon was observed previously in [30] during photocatalytic CSB decomposition in the *presence of ZnO-MgO composite.*

The kinetic equation of pseudo-first order, which is often used in photocatalysis in integral form, can be written as [17, 30, 55]:

$$\frac{C}{C_0} = e^{-kt},\tag{3}$$

where C_0 and C - initial and current dye concentrations (mM); t - duration of UV irradiation (min); and k - reaction rate constant (min^{-1}). The dependencies - ln(C/C$_0$) = f(t) calculated based on the experimental results (Figure 10a) are presented in Figure 10b. Experimental results don't correspond to equation (3) (R^2 < 0.9) (Figure 10b). Also, Figure 10 shows that the increase of Mn content in composites accelerates the discoloration of dye solutions, but it does not affect the behavior of kinetic dependences of this process.

3.6 Antibacterial Activity

Figure 11 shows the photo indicating the formation of zones free from the bacteria *Staphylococcus aureus ACC 209P* around the powder samples of ZnZrMn2. This image demonstrates

a significant difference in the size of these zones for various bacteria. Large zones free from the bacteria *Staphylococcus aureus ATCC 209P* are seen in Figure 11, indicating the high antibacterial activity of the ZnZrMn2 sample against these bacteria.
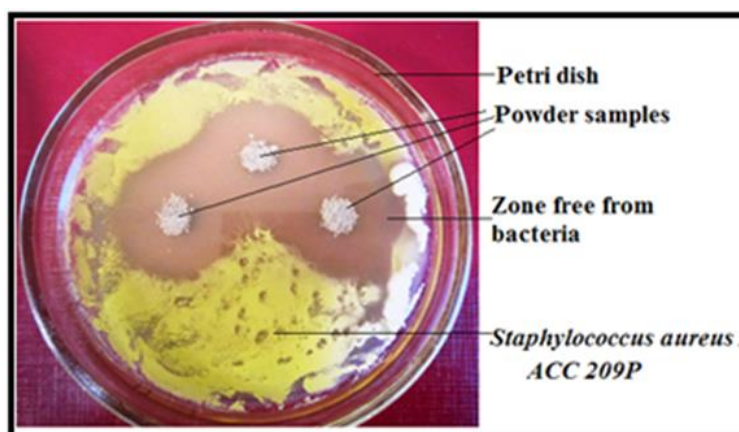

Figure 11 Photo demonstrating the formation of zones free from the bacteria *Staphylococcus aureus ATCC 209P* around powder samples ZnZrMn2.

4. Discussion

Experimental results obtained by XRD and SEM methods showed that prepared composites consist of small ZnO and ZrO_2 nanocrystals forming dispersed porous particles. This structure of materials provides effective contact with surrounding media and enhances their high photocatalytic and bactericidal properties.

The modification of the ZnO-ZrO_2 composite by Mn ions leads to the remarkable deformation of ZnO crystals due to the difference in the ionic radii of Zn^{2+} and Mn^{2+} ions. The growth of Mn content in the materials increases these changes in ZnO crystal cells. These structural changes can lead to the formation of different defects in ZnO crystals and affect the photocatalytic properties of the composites.

The study of luminescence spectra in the visible spectral range of obtained composites showed the presence of numerous emission peaks related to different structural defects of ZnO and ZrO_2 crystals. The observed luminescence band (λ_{max} = 1270 nm) characteristic for singlet oxygen [39] indicates its effective photogeneration by prepared nanocomposites under visible irradiation. The excited photon energy (3.06 eV) is lower than the band gap values of both central components of prepared composites (E_g^{ZnO} ~3.37 eV; E_g^{ZrO2} ~5.1 eV). Thus, it suggests that various defect centers are responsible for the observed photogeneration of singlet oxygen. It is worth noting that the presence of structural defects can significantly affect the photocatalytic and bactericidal properties of oxide materials [15, 16, 19]. Photocatalytic and bactericidal properties of obtained composites related to different active oxygen species (H_2O_2; ·OH; singlet oxygen and others). Experimental methods used in this article provide the possibility of studying the photogeneration of singlet oxygen only. Nevertheless, we think that the results obtained allow for the estimation of the general tendency of ROS photogeneration.

The experimental results of dye photocatalytic decomposition under UV irradiation shown in Figure 8a show that equation (2) describes the experimental data successfully (R^2 = 0.98). The

obtained k values were used to analyze the influence of the UV radiation intensity on the photocatalysis kinetics.

The non-linear dependencies of $k = f(I_{ex})$ observed in Figure 8b were described previously in [33, 40, 56]. Significant deviations from the linearity of the dependencies of $k = f(I_{ex})$ are attributed to the strong growth of recombination of photogenerated electron-hole pairs at high radiation intensity. Nevertheless, the results shown in Figure 9b indicate the possibility of a remarkable acceleration of photocatalytic dye decomposition by prepared composites using more intensive irradiation.

The observed discoloration of dye solutions during photocatalytic experiments under visible light irradiation (Figure 10b) is determined by both the photocatalytic dye decomposition and its adsorption on the surface of the composite powder. Therefore, the obtained experimental results shown in Figure 9 and Figure 10 suggest that dye adsorption is the main contributor to the solution discoloration during photocatalytic experiments under visible irradiation. This significant contribution of fast dye adsorption can be the possible reason for the inconsistent experimental results observed in equation (3).

The obtained experimental results show the excitation light source's significant effect on the prepared composites' photocatalytic activity. It is possible to suggest that this phenomenon is related to both the difference in the energies of the exciting photons and the ratio of the rates of dye adsorption and its photocatalytic decomposition.

In some previous works [52-54], the dye adsorption rate was relatively low ($k_a = 0.007$ min^{-1} [52]; $0.04 \div 0.08$ min^{-1} [53]; 0.014 min^{-1} [54]) and the rate of photocatalytic dye decomposition was significantly higher (f.e., $k = 0.069$ min^{-1} [54]). The input of adsorption in the dye solutions' discoloration was low in these studies [52-54]. In these cases, the slight decrease of the dye photocatalytic decomposition rate due to applying a light source with longer wavelength emission cannot change the ratio between dye adsorption rates and its photocatalytic decomposition remarkably. Correspondingly, the experimental data of photocatalysis rates described in [52-54] are well described by the pseudo-first-order kinetic equation (3).

In the present work, the adsorption rate is high enough ($k_{ads} = 0.017$ min^{-1}; Figure 7) and this process determines the dye solution discoloration during photocatalytic experiments using visible irradiation.

The scheme illustrating the influence of fast dye adsorption on the photocatalyst surface on the kinetics of the dye photocatalytic decomposition is shown in Figure 12. At the initial stage of the photocatalytic process, the photocatalyst surface is only partly filled by adsorbed dye molecules and light excitation of the photocatalyst and the dye decomposition proceeds effectively enough (Figure 12A). After filling the surface with the adsorbed dye, the effectiveness of photocatalyst excitation fails due to the shielding effect by the CSB molecules layer. This leads to a significant reduction of the photocatalysis rate and the rate constant becomes close to the low value observed at the photolysis of CSB in aqueous solutions without any photocatalytic additions (0.002 min^{-1} [54]).
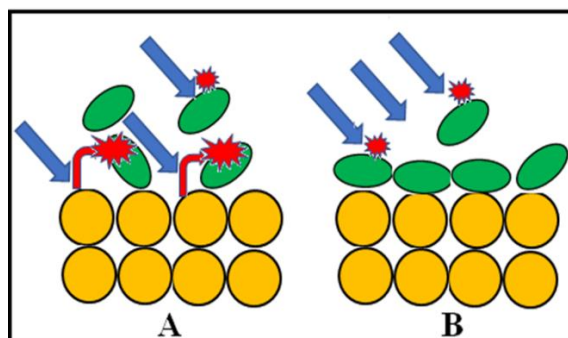
Figure 12 Illustrates the influence of fast dye adsorption on the photocatalyst surface on the kinetics of the dye photocatalytic decomposition. A) Initial process, partly filled surface. B) Fully filled surface.

It is worth noticing that this phenomenon is observed at the photocatalysis using visible irradiation. In this case, the rate of the photocatalytic process is lower or comparable to the dye adsorption rate. The rate of dye photocatalytic decomposition is significantly higher when applying UV radiation for photocatalyst excitation, and the photocatalyst surface does not have time to become covered with dye molecules.

Thus, we can conclude that the photocatalytic process's kinetics depend on the wavelength and power density of the used light source, as well as the ratio between the rates of dye photocatalytic decomposition and its adsorption.

Prepared composites demonstrated superior antibacterial activity against the bacteria *Staphylococcus aureus ATCC 209P*. The results of antibacterial tests of the prepared materials and some literature data [33, 34] are given in Table 3. The powder composites $ZnO-SnO_2$ and $ZnO-SnO_2$-Ag were prepared previously by the same polymer-salt method and were evaluated under similar conditions. The comparison of the presented data shows that $ZnO-ZrO_2$ materials demonstrate higher antibacterial activity against the bacteria *Staphylococcus aureus ATCC 209P* than the powders prepared earlier.

Table 3 The results of antibacterial tests of prepared materials and literature data.

Sample	Thickness of the zone free from bacteria, mm	Reference
Mn0	11	Present study
Mn0.5	16	Present study
Mn1	11	Present study
Mn2	11	Present study
ZnO	7	[33]
ZnO 97.4 mol.% + SnO_2 2.6 mol.%	7	[33]
ZnO 93.6 mol.% + SnO_2 6.4 mol.%	8	[33]
ZnO 91.1 mol.% + SnO_2 8.9 mol.%	9	[33]
ZnO 87.5 mol.% + SnO_2 12.5 mol.%	9	[33]
ZnO 87.6 mol.% + SnO_2 11.8 mol.% + Ag 0.6 mol.%	7	[34]
ZnO 87.1 mol.% + SnO_2 11.7 mol.% + Ag 1.2 mol.%	5	[34]
ZnO 86.5 mol.% + SnO_2 11.7 mol.% + Ag 1.8 mol.%	7	[34]

ZnO 67.2 mol.% + SnO$_2$ 9.0 mol.% + Ag 23.8 mol.%	8	[34]

Antibacterial tests were conducted under natural lighting conditions, and visible irradiation had some input in the bactericidal action of the prepared composites. Different structural defects have electronic levels in the band gaps of ZnO, and ZrO$_2$ crystals absorb light in the near UV and visible spectral range. Compared to defect-free crystals, this light absorption can be followed by additional ROS generation by the composites, which increases their antibacterial effect. This corresponds to our samples' observed high antibacterial activity against the bacteria *Staphylococcus aureus ATCC 209 P* (Figure 10 and Table 3)*.*

Based on experimental data,, it is possible to conclude that the antibacterial effectiveness of Mn-doped ZnO-ZrO$_2$ composites, which have many different defects in their structures, depends significantly on the bacteria structure.

5. Conclusions

The non-isothermal polymer-salt method synthesized mn-doped ZnO-ZrO$_2$ composites with high antibacterial properties. The crystal structures and morphologies of the materials were studied using XRD and SEM analysis. The obtained porous composites consist of small (~9 nm) hexagonal ZnO crystals and ZrO$_2$ nanocrystals. The embedding of Mn ions into the structure of ZnO expands and deforms its crystal cells. Measurements of the photoluminescence spectra in the visible spectral range showed the presence of many different intrinsic defects (oxygen vacancies, interstitials Zn ions, etc.) in the structures of ZnO and ZrO$_2$ crystals.

It was found that the obtained composites demonstrate a solid ability to generate singlet oxygen under visible (λ_{ex} = 405 nm) irradiation. The dependence of the concentration of photogenerated singlet oxygen on the intensity of excited light is non-linear. This is due to the significant increase in the recombination of photogenerated electron-hole pairs in the composites with the growth of the exciting radiation intensity.

A pseudo-first-order kinetic equation describes the kinetics of photocatalytic decomposition of the diazo dye Chicago Sky Blue under UV irradiation in the presence of Mn-doped ZnO-ZrO$_2$ composites. On the contrary, at the application of visible irradiation, the kinetics of the discoloration of the same solutions with these composites is determined by the adsorption of dye molecules on the powder surface. The increase of Mn concentration in the composites enhances their photocatalytic activity. The rate constant of the photocatalytic reaction increases from 0.012 to 0.035 min^{-1} with increasing Mn concentration.

Mn-doped ZnO-ZrO$_2$ composites demonstrate superior antibacterial activity against the gram-positive bacteria *Staphylococcus aureus ATCC 209 P*. The value of the zone without bacteria when using the disk method ranges from 11 to 16 mm, which is significantly higher (up to 2 times) than in similar studies.

The experimental results demonstrate that Mn-doped ZnO-ZrO$_2$ composites are promising for practical medical and environmental applications.

Author Contributions

Conceptualization, Evstropiev S.K.; Validation, Karavaeva A.V.; Project Administration, Nikonorov N.V.; Investigation, Bagrov I.V.; Investigation, Shelemanov A.V.; Investigation, Portnova K.A. All authors have read and agreed to the published version of the manuscript.

Funding

Competing Interests

The authors have declared that no competing interests exist.

References

1. Vatansever F, de Melo WC, Avci P, Vecchio D, Sadasivam M, Gupta A, et al. Antimicrobial strategies centered around reactive oxygen species-bactericidal antibiotics, photodynamic therapy, and beyond. FEMS Microbiol Rev. 2013; 37: 955-989.
2. Li Y, Zhang W, Niu J, Chen Y. Mechanism of photogenerated reactive oxygen species and correlation with the antibacterial properties of engineered metal-oxide nanoparticles. ACS Nano. 2012; 6: 5164-5173.
3. Lobo V, Patil A, Phatak A, Chandra N. Free radicals, antioxidants and functional foods: Impact on human health. Pharmacogn Rev. 2010; 4: 118-126.
4. Bell S, Will G, Bell J. Light intensity effects on photocatalytic water splitting with a titania catalyst. Int J Hydrogen Energy. 2013; 38: 6938-6947.
5. Huang Z, Zheng X, Yan D, Yin G, Liao X, Kang Y, et al. Toxicological effect of ZnO nanoparticles based on bacteria. Langmuir. 2008; 24: 4140-4144.
6. Kardeş M, Yatmaz HC, Öztürk K. ZnO nanorods grown on flexible polyurethane foam surfaces for photocatalytic azo dye treatment. ACS Appl Nano Mater. 2023; 6: 6605-6613.
7. Padmavathy N, Vijayaraghavan R. Enhanced bioactivity of ZnO nanoparticles-an antimicrobial study. Sci Technol Adv Mater. 2008; 9: 035004.
8. Evstropiev SK, Karavaeva AV, Dukelskii KV, Evstropyev KS, Nikonorov NV, Kolobkova EV. Transparent $ZnO-Y_2O_3$ coatings: Bactericidal effect in the lighting and in the darkness. Ceram Int. 2018; 44: 9091-9096.
9. Raghupathi KR, Koodali RT, Manna AC. Size-dependent bacterial growth inhibition and mechanism of antibacterial activity of zinc oxide nanoparticles. Langmuir. 2011; 27: 4020-4028.
10. Yang S, Lian G. ROS and diseases: Role in metabolism and energy supply. Mol Cell Biochem. 2020; 467: 1-12.
11. Nosaka Y, Nosaka AY. Generation and detection of reactive oxygen species in photocatalysis. Chem Rev. 2017; 117: 11302-11336.
12. Khomutinnikova L, Evstropiev S, Meshkovskii I, Bagrov I, Kiselev V. Ceramic $ZnO-SnO_2-Fe_2O_3$ powders and coatings-effective photogenerators of reactive oxygen species. Ceramics. 2023; 6: 886-897.
13. Hamrouni A, Moussa N, Parrino F, Di Paola A, Houas A, Palmisano L. Sol-gel synthesis and photocatalytic activity of $ZnO-SnO_2$ nanocomposites. J Mol Catal A Chem. 2014; 390: 133-141.

14. Pirzada BM, Mir NA, Qutub N, Mehraj O, Sabir S, Muneer M. Synthesis, characterization and optimization of photocatalytic activity of TiO_2/ZrO_2 nanocomposite heterostructures. Mater Sci Eng B. 2015; 193: 137-145.

15. Bhatia S, Verma N. Photocatalytic activity of ZnO nanoparticles with optimization of defects. Mater Res Bull. 2017; 95: 468-476.

16. Liu Y, Wang Y, Zhen W, Wang Y, Zhang S, Zhao Y, et al. Defect modified zinc oxide with augmenting sonodynamic reactive oxygen species generation. Biomaterials. 2020; 251: 120075.

17. Al-Rawashdeh NA, Allabadi O, Aljarrah MT. Photocatalytic activity of graphene oxide/zinc oxide nanocomposites with embedded metal nanoparticles for the degradation of organic dyes. ACS Omega. 2020; 5: 28046-28055.

18. Kiriarachchi HD, Abouzeid KM, Bo L, El-Shall MS. Growth mechanism of sea urchin ZnO nanostructures in aqueous solutions and their photocatalytic activity for the degradation of organic dyes. ACS Omega. 2019; 4: 14013-14020.

19. Rani V, Sharma A, Kumar A, Singh P, Thakur S, Singh A, et al. ZrO_2-based photocatalysts for wastewater treatment: From novel modification strategies to mechanistic insights. Catalysts. 2022; 12: 1418.

20. Lanjwani MF, Tuzen M, Khuhawar MY, Saleh TA. Trends in photocatalytic degradation of organic dye pollutants using nanoparticles: A review. Inorg Chem Commun. 2024; 159: 111613.

21. Akilandeswari S, Rajesh G, Govindarajan D, Thirumalai K, Swaminathan M. Efficacy of photoluminescence and photocatalytic properties of Mn doped ZrO_2 nanoparticles by facile precipitation method. J Mater Sci Mater Electron. 2018; 29: 18258-18270.

22. Abu-Dalo M, Jaradat A, Albiss BA, Al-Rawashdeh NA. Green synthesis of TiO_2 NPs/pristine pomegranate peel extract nanocomposite and its antimicrobial activity for water disinfection. J Environ Chem Eng. 2019; 7: 103370.

23. Gurushantha K, Renuka L, Anantharaju KS, Vidya YS, Nagaswarupa HP, Prashantha SC, et al. Photocatalytic and photoluminescence studies of ZrO_2/ZnO nanocomposite for LED and waste water treatment applications. Mater Today Proc. 2017; 4: 11747-11755.

24. Długosz O, Szostak K, Banach M. Photocatalytic properties of zirconium oxide-zinc oxide nanoparticles synthesised using microwave irradiation. Appl Nanosci. 2020; 10: 941-954.

25. Uribe López MC, Alvarez Lemus MA, Hidalgo MC, López González R, Quintana Owen P, Oros-Ruiz S, et al. Synthesis and characterization of $ZnO-ZrO_2$ nanocomposites for photocatalytic degradation and mineralization of phenol. J Nanomater. 2019; 2019: 1015876.

26. Aghabeygi S, Khademi-Shamami M. ZnO/ZrO_2 nanocomposite: Sonosynthesis, characterization and its application for wastewater treatment. Ultrason Sonochem. 2018; 41: 458-465.

27. Precious Ayanwale A, Reyes-López SY. ZrO_2-ZnO nanoparticles as antibacterial agents. ACS Omega. 2019; 4: 19216-19224.

28. Bilgili O. The effects of Mn doping on the structural and optical properties of ZnO. Acta Phys Pol A. 2019; 136: 460-466.

29. Chen W, Zhao LF, Wang YQ, Miao JH, Liu S, Xia ZC, et al. Magnetism in Mn-doped ZnO bulk samples. Solid State Commun. 2005; 134: 827-830.

30. Bulyga DV, Evstropiev SK. Kinetics of adsorption and photocatalytic decomposition of a diazo dye by nanocomposite ZnO-MgO. Opt Spectrosc. 2022; 130: 1176.

31. Omri K, Lemine OM, El Ghoul J, El Mir L. Sol-gel synthesis and room temperature ferromagnetism in Mn doped ZnO nanocrystals. J Mater Sci Mater Electron. 2015; 26: 5930-5936.

32. Jeba R, Radhika S, Padma CM, Ascar Davix X. Structural, optical, thermal, magnetic properties of zirconia nano-rods and their photocatalytic and antimicrobial properties. J Water Environ Nanotechnol. 2021; 6: 252-264.

33. Evstropiev SK, Karavaeva AV, Vasilyev VN, Nikonorov NV, Aseev VA, Dukelskii KV, et al. Bactericidal properties of ZnO-SnO$_2$ nanocomposites prepared by polymer-salt method. Mater Sci Eng B. 2021; 264: 114877.

34. Volynkin VM, Danilovich DP, Evstropiev SK, Dukel'skii KV, Senchik KY, Sadovnichii RV, et al. Synthesis of photoactive ZnO-SnO$_2$-Ag (AgCl) nanomaterials for medical and ecological applications and study of their structure and properties. Opt Spectrosc. 2021; 129: 746-753.

35. Gavrilova MA, Gavrilova DA, Evstropiev SK, Nikonorov NV. Structure, spectral and photocatalytic properties of porous ZnO nanopowders modified by oxide compounds of manganese. Russ J Inorg Chem. doi: 10.1134/S0036023623602994.

36. Schliephake K, Mainwaring DE, Lonergan GT, Jones IK, Baker WL. Transformation and degradation of the disazo dye Chicago sky blue by a purified laccase from pycnoporus cinnabarinus. Enzyme Microb Technol. 2000; 27: 100-107.

37. Karzel H, Potzel W, Köfferlein M, Schiessl W, Steiner M, Hiller U, et al. Lattice dynamics and hyperfine interactions in ZnO and ZnSe at high external pressures. Phys Rev B. 1996; 53: 11425.

38. Kisi EH, Elcombe MM. U parameters for the wurtzite structure of ZnS and ZnO using powder neutron diffraction. Acta Crystallogr C. 1989; 45: 1867-1870.

39. Nosaka Y, Daimon T, Nosaka AY, Murakami Y. Singlet oxygen formation in photocatalytic TiO$_2$ aqueous suspension. Phys Chem Chem Phys. 2004; 6: 2917-2918.

40. Deng Y. Developing a langmuir-type excitation equilibrium equation to describe the effect of light intensity on the kinetics of the photocatalytic oxidation. Chem Eng J. 2018; 337: 220-227.

41. Smits K, Grigorjeva L, Millers D, Sarakovskis A, Grabis J, Lojkowski W. Intrinsic defect related luminescence in ZrO$_2$. J Lumin. 2011; 131: 2058-2062.

42. Liang J, Deng Z, Jiang X, Li F, Li Y. Photoluminescence of tetragonal ZrO$_2$ nanoparticles synthesized by microwave irradiation. Inorg Chem. 2002; 41: 3602-3604.

43. Vempati S, Mitra J, Dawson P. One-step synthesis of ZnO nanosheets: A blue-white fluorophore. Nanoscale Res Lett. 2012; 7: 470.

44. Horti NC, Kamatagi MD, Nataraj SK, Sannaikar MS, Inamdar SR. Photoluminescence properties of zirconium oxide (ZrO$_2$) nanoparticles. AIP Conf Proc. 2020; 2274: 020002.

45. Zeng H, Duan G, Li Y, Yang S, Xu X, Cai W. Blue luminescence of ZnO nanoparticles based on non-equilibrium processes: Defect origins and emission controls. Adv Funct Mater. 2010; 20: 561-572.

46. Wang Z, Yang B, Fu Z, Dong W, Yang Y, Liu W. UV-blue photoluminescence from ZrO$_2$ nanopowders prepared via glycine nitrate process. Appl Phys A. 2005; 81: 691-694.

47. Perevalov TV, Gulyaev DV, Aliev VS, Zhuravlev KS, Gritsenko VA, Yelisseyev AP. The origin of 2.7 eV blue luminescence band in zirconium oxide. J Appl Phys. 2014; 116: 244109.

48. Das D, Mondal P. Photoluminescence phenomena prevailing in c-axis oriented intrinsic ZnO thin films prepared by RF magnetron sputtering. RSC Adv. 2014; 4: 35735-35743.

49. Guo L, Yang S, Yang C, Yu P, Wang J, Ge W, et al. Highly monodisperse polymer-capped ZnO nanoparticles: Preparation and optical properties. Appl Phys Lett. 2000; 76: 2901-2903.

50. D'Alelio GF, Underwood JW. Diazine derivatives. Alexandria, VA: United States Patent Office; 1942; No. 436,249. Available from: https://patentimages.storage.googleapis.com/e8/a1/34/df7983c8a1a4c9/US2324369.pdf.

51. Lin YH, Weng CH, Tzeng JH, Lin YT. Adsorption and photocatalytic kinetics of visible-light response N-doped TiO_2 nanocatalyst for indoor acetaldehyde removal under dark and light conditions. Int J Photoenergy. 2016; 2016: 3058429.

52. Shelemanov A, Tincu A, Evstropiev S, Nikonorov N, Vasilyev V. Cu-doped porous $ZnO-ZnAl_2O_4$ nanocomposites synthesized by polymer-salt method for photocatalytic water purification. J Compos Sci. 2023; 7: 263.

53. Khomutinnikova LL, Evstropiev SK, Danilovich DP, Meshkovskii IK, Bulyga DV. Structural engineering of photocatalytic $ZnO-SnO_2-Fe_2O_3$ composites. J Compos Sci. 2022; 6: 331.

54. Gavrilova M, Gavrilova D, Kondrashkova I, Evstropiev S. Structural engineering of nanocrystalline $Zn_{0.5}Ni_{0.5}Fe_2O_4$ synthesized by auto combustion method through the use of different organic reducing compounds and its effect on magnetic and photocatalytic properties. J Mater Sci Mater Electron. 2023; 34: 1644.

55. Konstantinou IK, Albanis TA. TiO_2-assisted photocatalytic degradation of azo dyes in aqueous solution: Kinetic and mechanistic investigations: A review. Appl Catal B. 2004; 49: 1-14.

56. Puma GL, Salvadó-Estivill I, Obee TN, Hay SO. Kinetics rate model of the photocatalytic oxidation of trichloroethylene in air over TiO_2 thin films. Sep Purif Technol. 2009; 67: 226-232.